Supplementary Information for Huismans and Beaumont.

1. Supplementary Figure and Information on the Iberia-Newfoundland conjugate margin system

a) Type I Non Volcanic Margins Iberia - Newfoundland
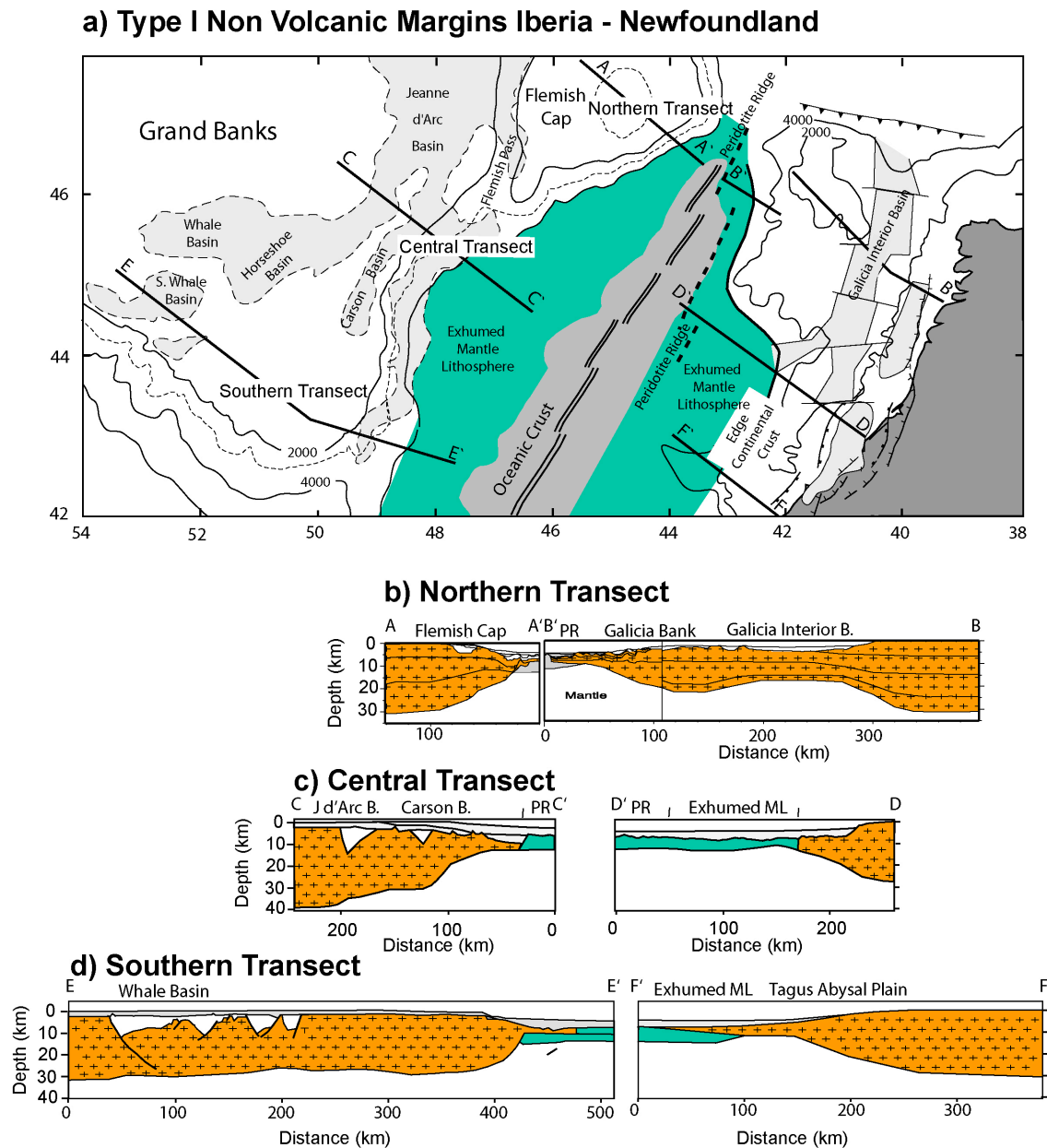

Figure A1. The Iberia - Newfoundland conjugate margin system and crustal cross sections. **a)** Map of the Cretaceous Central Atlantic restored to magnetic anomaly M0 time (~121 *Ma*) based on reconstruction pole of Srivastava[1] with Newfoundland fixed to present geographic coordinates. **b)**, **c)**, **d)** Northern, Central and Southern crustal conjugate cross sections based on seismic reflection data, and gravity inversion for the Iberia-Newfoundland margin system (Northern transect[2-4], Central Transect[5-7], Southern

Transect[5-6,8]. Note older exterior basins, short crustal thinning length scale adjacent to oceanic crust, thin crustal wedge on top of mantle lithosphere, and exhumed mantle lithosphere in ocean-continent-transition zone.

2. Supplementary Figures and Information on the West African margin of the Central South Atlantic

Interpreted seismic cross-sections of the north Angolan to south Gabon West African passive margins[9-11], including Figure 1 in the paper (bottom panel), that indicate similarity of structural and sedimentary features along strike on a 1000 km scale.
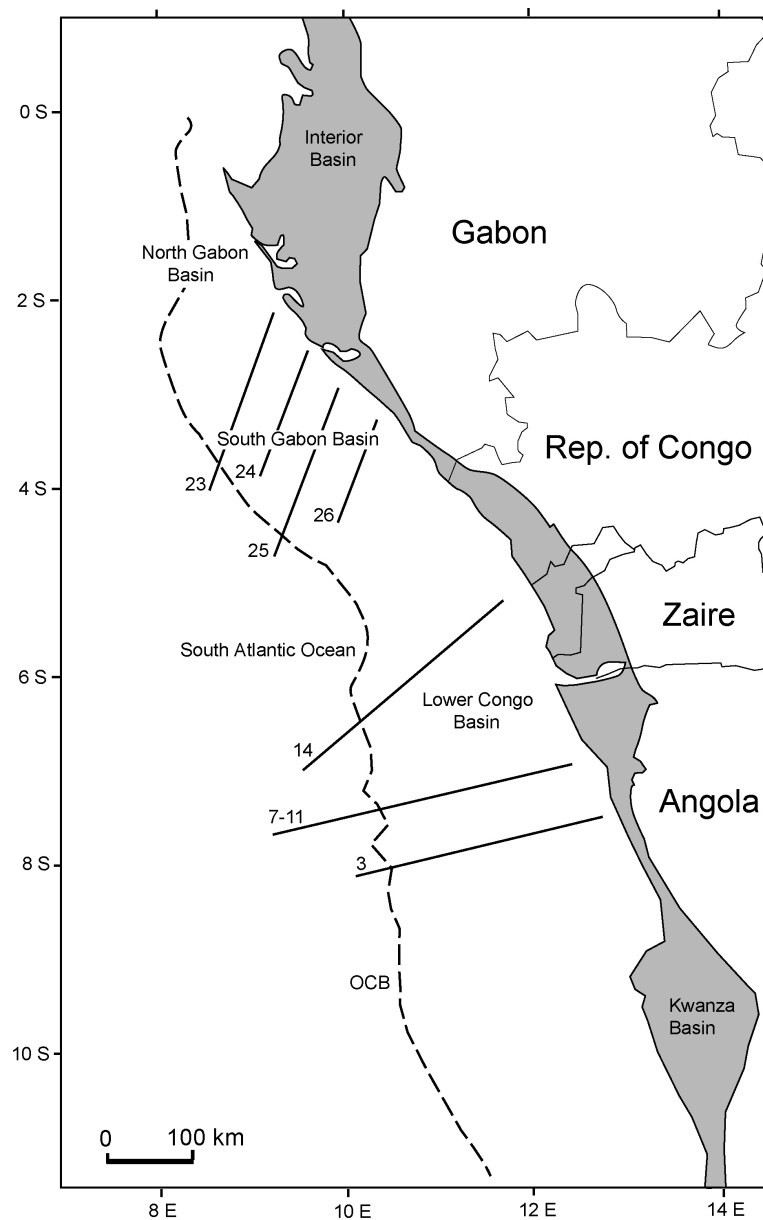

Figure A2. Map of West African north Angolan to south Gabon margins with locations of seismic cross-sections shown in Figure A3. OCB is the ocean continent boundary.
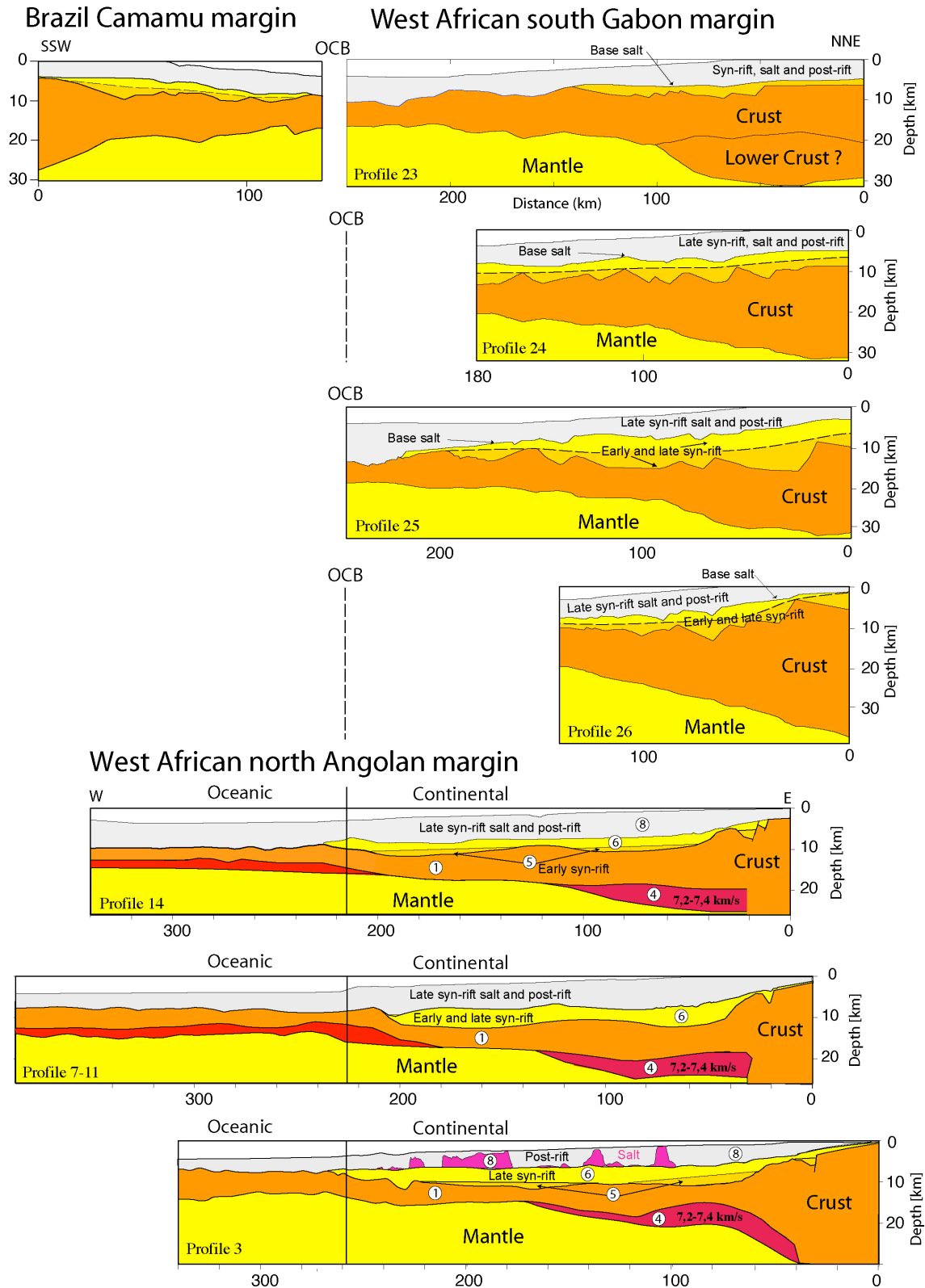
Brazil Camamu margin

West African south Gabon margin

West African north Angolan margin

Figure A3. Crustal cross sections from the West African North Angolan to South Gabon margins (modified after[9-11]). The crustal cross sections show wide regions of thin crust, thin early syn-rift deposits, thicker undeformed late syn-rift deposits, post-rift, and in the Angola sections an intermediate velocity body of unknown origin at the base of the crust. South Gabon[11] and

Camamu[10] sections have been depth converted from original TWTT
sections. The boundary between early and late syn-rift in these sections is
not well imaged and approximately given by dashed line. OCB is ocean
continent boundary. In these interpretations the mantle is interpreted to be
oceanic/standard continental (yellow) but may contain a region of
underplated cratonic lower continental lithosphere which would be coloured
light green (see Figure 3). See main text for explanation of numbers.
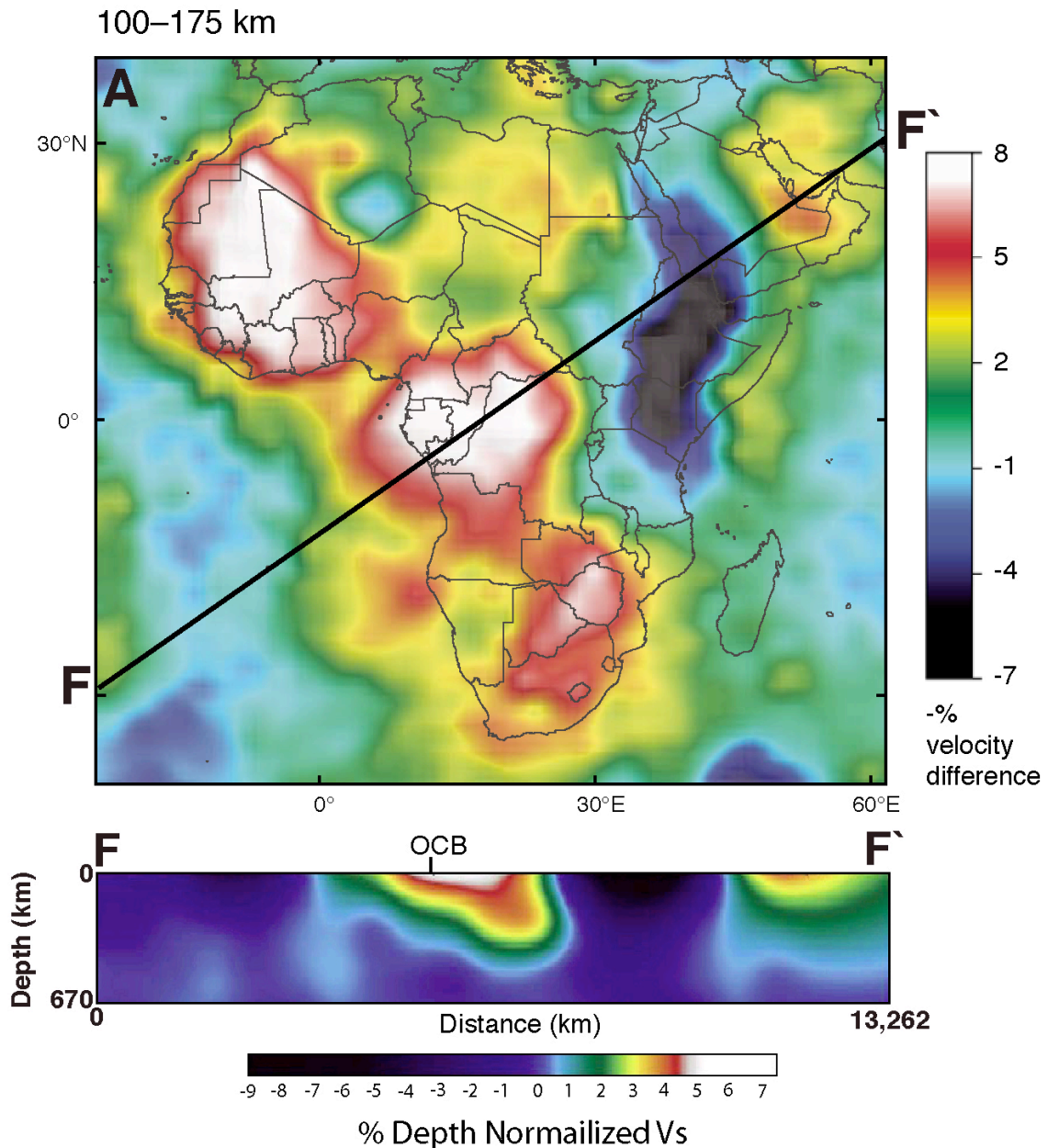
100–175 km

Figure A4. S wave tomography of Africa 100-175 km depth slice (after[12]).
Note positive velocity anomaly extending from the Congo craton under the
passive margin into the oceanic domain indicating possible lower
lithosphere flow into the oceanic domain.

3. Supplementary Methods

We use an Arbitrary Lagrangian-Eulerian (ALE) finite element method for the solution of thermo-mechanically coupled, plane-strain, incompressible viscous-plastic creeping flows[13-15] to investigate extension of a layered lithosphere with frictional-plastic and thermally activated power-law viscous rheologies (Figure A6).

When the state of stress is below the frictional-plastic yield the flow is viscous and is specified by temperature-dependent non-linear power law rheologies based on laboratory measurements on 'wet' quartzite[16] and 'wet' and 'dry' olivine[17]. The effective viscosity, η, in the power-law rheology is of the general form:

$$\eta = f \, A^{-\frac{1}{n}} (\dot{I}_2^{/})^{(1-n)/2n} \exp\left[\frac{Q+Vp}{nRT}\right] \tag{1}$$

where $\dot{I}_2^{/}$ is the second invariant of the deviatoric strain rate tensor ($\frac{1}{2}\dot{\varepsilon}_{ij}^{/}\dot{\varepsilon}_{ij}^{/}$), n is the power law exponent, A is the pre-exponential scaling factor, f is a scaling factor representing viscous weakening or strengthening, Q is the activation energy, V is the activation volume, which makes the viscosity dependent on pressure, p, T is the absolute temperature, R is the universal gas constant, and $\dot{\varepsilon}_{ij}^{/}$ is the deviatoric strain rate tensor. A (converted from the laboratory strain geometry to the tensor invariant form), n, Q and V are derived from the laboratory experiments and the parameter values are listed in Table 1. Note setting $V = 0$ for the quartzite flow law does not lead to significant errors because the pressure in the crust is low.

The effective viscosity of quartz dominated rocks is characterised by large uncertainties. Figure A5 plots predicted effective viscosity as a function of temperature for a range of wet quartz flow laws (based on[16], table 3). The reference parameter values for wet quartz used here, listed in Table 1 (labelled GT in Figure A5) represent a moderately strong viscous mid and lower crust. The models described here use values of the reference quartz flow law, which are scaled by factor f. The scale values are designed to produce crust with strong and weak regions (Fig. A6c). In Model I strong crust with no viscous flow is achieved by increasing $\eta_{wet\ quartz}$ with scale factor f=30. This can be interpreted to represent crust controlled by viscous flow of 'dry' feldspar. In Models II-A

and II-C weak crust is achieved with a scale factor f=0.02 which can be interpreted as viscous flow controlled by a weaker quartz rheology (Fig A5), an effect of viscous strain weakening, or a combination of these factors. Strong cratonic crust is achieved with a scale factor f=100.
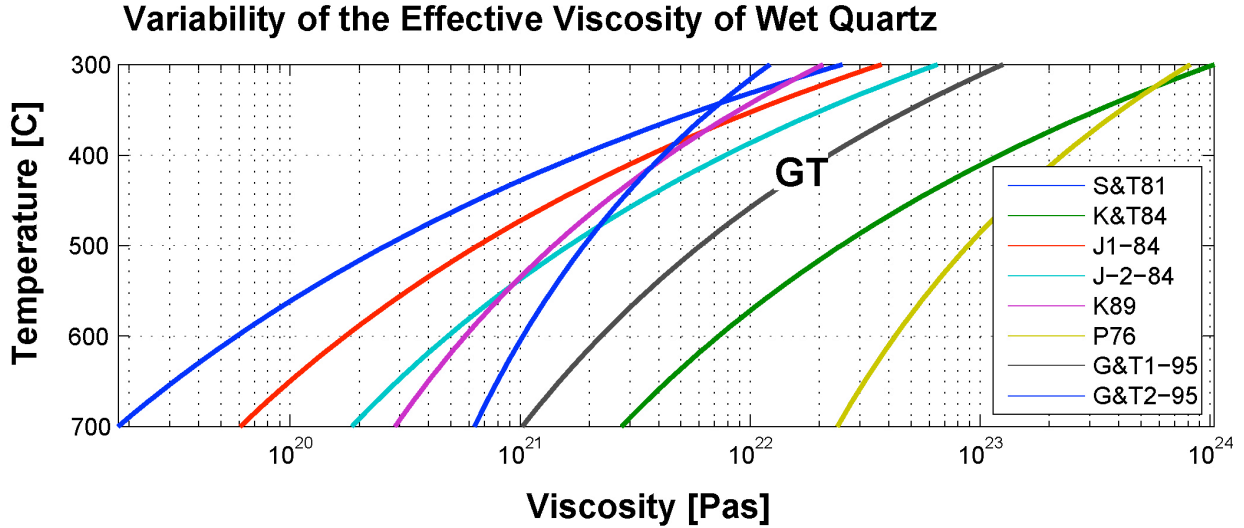
Variability of the Effective Viscosity of Wet Quartz

Figure A5. Dependence of the effective viscosity of quartz on temperature for a constant strain rate of 10^{-15} s^{-1} based on laboratory measurements. The uncertainty is such that the effective viscosity varies over more than 2 orders of magnitude. Laboratory data based on Gleason and Tullis (1995, table 3). GT is the reference flow law used here.

Frictional-plastic yielding is modelled with a pressure-dependent Drucker-Prager yield criterion, which is equivalent to the Coulomb yield criterion for incompressible deformation in plane-strain. Yielding occurs when:

$$\sigma_y = (J_2^{/})^{1/2} = C\cos\phi_{eff} + p\,Sin\phi_{eff} \tag{2}$$

where $J_2^{/} = \frac{1}{2}\sigma_{ij}^{/}\sigma_{ij}^{/}$ is the second invariant of the deviatoric stress, $\sigma_{ij}^{/}$ is the deviatoric stress tensor, ϕ_{eff} is the effective internal angle of friction, $p\sin(\phi_{eff}) = (p - p_f)\sin(\phi)$ and p_f is the pore fluid pressure, and C is the cohesion. With appropriate choices of C and ϕ_{eff} this yield criterion can approximate frictional sliding in rocks and the effect of pore-fluid pressures. Plastic flow is incompressible. Strain softening is introduced by a

linear decrease of $\phi_{eff}(\varepsilon)$ from 15°-2° (Figure A6d and Table 1). Note that $\phi_{eff}(\varepsilon) \sim 15°$

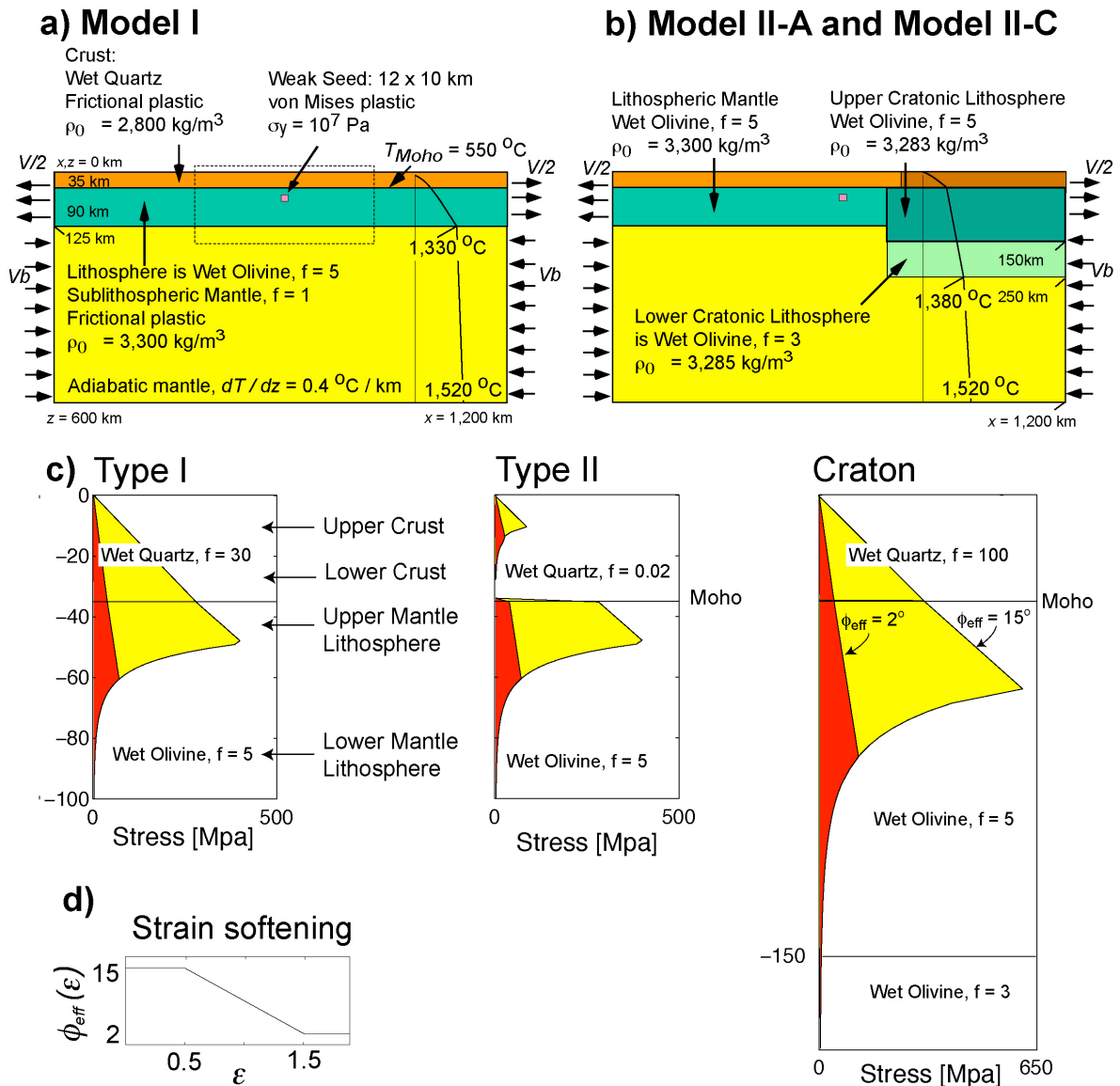corresponds to the effective ϕ when the pore fluid pressure is approximately hydrostatic.

Figure A6. Numerical model design. **a**) Model I and II initial crust and mantle

lithosphere layer thicknesses are respectively 35 *km* and 85 *km*. **b**) Model II-C

cratonic lithosphere (right part of model) initial crust and mantle lithosphere

layer thicknesses are respectively 35 *km* and 215 *km*. Total extension velocity

for Model I, $V = 0.5$ *cm a⁻¹*, for Model II-A and Model II-C, $V = 1.5$ *cm a⁻¹*.

These are reference velocity values and the model results are similar when the

values vary by +/- 30%. Materials deform viscously except when the material

is at plastic yield. **c**) Rheological stratification for Models I, II-A, and II-C for

a nominal strain rate of 10^{-14} *s⁻¹*. Materials listed are reference materials and

may be modified significantly by scaling by f. **d**) Strain softening of frictional-plastic rheology is a function of total strain; a linear decrease of $\phi_{eff}(\varepsilon)$ from 15°-2° over a strain range 0.5-1.5, where ε = second invariant of strain.

In addition to solving the equilibrium equations for viscous-plastic flows in two dimensions, we also solve for the thermal evolution of the model. The mechanical and thermal systems are coupled through the temperature dependence of viscosity and density and are solved sequentially during each model time step. The initial temperature field for Models I and II-A is laterally uniform, and increases with depth from the surface, $T_0 = 0$ °C, to base of crust, $T_m = 550$ °C, following a stable geotherm for uniform crustal heat production, $A_R = 0.9$ $\mu W/m^3$ and a basal heat flux, $q_m = 19.5$ mW/m^2. Model I and II geothermal gradients, 8.6 °C/km, and 0.4 °C/km (adiabatic) are uniform in the mantle lithosphere and sub-lithospheric mantle. Adiabatic heating and cooling are taking into account. Thermal boundary conditions are specified basal temperature, 1520 °C, and insulated lateral boundaries. Thermal diffusivity, $\kappa = k/\rho c_p = 10^{-6}$ m^2/s. For Model II-C the initial temperature field in the reference lithosphere is the same as in models I and II-A. In the cratonic part of the model temperature increases linearly from about $T = 480$ °C at the Moho to $T = 1380$ °C at the base of the cratonic lithosphere at $z = 250$ km. The steady state geothermal gradient in the cratonic mantle lithosphere was lowered by increasing the thermal diffusivity to respectively $\kappa_{cml} = 2.24$ x 10^{-6} m^2/s, and $\kappa_{slm} = 21.5$ x 10^{-6} m^2/s thereby achieving a temperature of 1380 °C at the base of the cratonic lithosphere. Densities of crust and mantle at 0 °C are, respectively, $\rho_{0c} = \rho_c(T_0) = 2800$ kg/m^3 and $\rho_{0m} = \rho_m(T_0) = 3300$ kg/m^3, and depend on temperature with a volume coefficient of thermal expansion $\alpha_T = 2$ x 10^{-5} /°C, $\rho(T) = \rho_0$ [1 - α_T (T-T_0)]. Cratonic lithosphere is depleted such that the upper cratonic mantle has $\rho_m(T_0) = 3283$ kg/m^3 (a compositional density anomaly of -17 kg/m^3) and lower cratonic mantle lithosphere has $\rho_m(T_0) = 3285$ kg/m^3 (a compositional density anomaly of -15 kg/m^3).

Table 1. Model Parameters Values.

Parameter	Symbol	Value
Rheological Parameters		
Angle of internal friction	$\phi(\varepsilon)$ *and strain range of softening,* $(\varepsilon = I_2^{/})$	15° - 2°, 0.5-1.5
Cohesion	C	0 *Pa*
Wet Quartz[16]		
Power law exponent	N	4.0
Activation Energy	Q	223 x 10³ *J/mol*
Initial Constant*	A	8.5737 x 10⁻²⁸ *Pa⁻ⁿ/s*
Activation Volume	V	0 *m³/mol*
Crust Weakening factor	f_c	0.02, 30, 100
Wet Olivine[17]		
Power law exponent	n	3.0
Activation Energy	Q	430 x 10³ *J/mol*
Initial Constant*	A	1.7578 x 10⁻¹⁴ *Pa⁻ⁿ/s*
Activation Volume	V	15 x 10⁻⁶ *m³/mol*
Mantle lithosphere weakening factor	f_{ml}	5
Sub lithosphere weakening factor	f_{slm}	1
Upper cratonic mantle lithosphere weakening factor	f_{ucm}	5
Lower cratonic mantle lithosphere weakening factor	f_{lcm}	3
Universal Gas Constant	R	8.3144 *J/mol/°C*
Thermal Parameters		
Diffusivity	κ	1 x 10⁻⁶ *m²/s*
Diffusivity sub lithospheric mantle	κ_{slm}	21.5 x 10⁻⁶ *m²/s*
Diffusivity cratonic lithosphere mantle	κ_{cml}	2.24 x 10⁻⁶ *m²/s*
Crustal radioactive heat production	A_R	0.9 x 10⁻⁶ *W/m³*
Volume coefficient of thermal expansion	α_T	2 x 10⁻⁵ /*°C*
Surface Temperature	T_0	0 *°C*
Standard Lithosphere		
Initial Moho Temperature	T_m	550 *°C*
Base Lithosphere Temperature	T_l	1330 *°C*
Cratonic Lithosphere		
Initial Cratonic Moho Temperature	T_{cm}	480 *°C*
Base Cratonic Lithosphere Temperature	T_{cml}	1380 *°C*
Basal Temperature	T_a	1520 *°C*
Densities (T_0 = 0 ºC)		

Crustal density	$\rho_c(T_0)$	2800 kg/m^3
Mantle lithosphere density	$\rho_m(T_0)$	3300 kg/m^3
Sub lithospheric mantle density	$\rho_a(T_0)$	3300 kg/m^3
Upper cratonic mantle lithosphere density	$\rho_{ucm}(T_0)$	3283 kg/m^3
Lower cratonic mantle lithosphere density	$\rho_{lcm}(T_0)$	3285 kg/m^3
Dimensions and Boundary Condition		
Base of crust		35 km
Base mantle lithosphere		125 km
Base cratonic mantle lithosphere		250 km
Base upper mantle		600 km
Extension velocity	$V/2$	0.25 and 0.75 $cm\ a^{-1}$ (half rate)
Top boundary condition		Stress free surface
Side boundary conditions		Free slip, normal velocity V
Basal boundary conditions		Free slip, zero normal velocity

[*]Values of A have been converted from the experimental values to values appropriate for tensor invariant conditions.

4) Preliminary Comments on Observed and Model Subsidence, Bathymetry and Sediment Thickness

In the numerical models the surface of the crust is loaded by sediment (density 2300 kg/m^3) and water, which in combination fill the model to sea level. The development of model bathymetry (near the rift axis) and sediment thickness elsewhere on the margins illustrates the model subsidence. The movies show this behaviour in the context of the extension and thinning of the lithosphere and are best viewed at high magnification in, for example, Windows Picture and Fax Viewer. We use these results to contrast the subsidence of Type I and Type II margins. (High quality .pdf graphic images available at http://sopalepc.ocean.dal.ca/extensional_Tectonics/Huismans_Beaumont_N_Supplementary_Figs).

Type I Margins

A particular characteristic of the Iberia-Newfoundland conjugate margins is the shallow paleobathymetry(<800 m) inferred for deposition of Tithonian sediments drilled at ODP sites 901, 1065 and 1069 and recently reviewed by Peron-Pinvidic and Manatschal (2009)[18]. Lower Valanginian nannofossil chalks at site 1069 are similar, indicating

deposition under outer shelf/upper slope conditions no deeper than 1500 m[19]. The inferred bathymetry may be anomalous depending on whether these locations correspond to positions where the crust had already been thinned substantially, and therefore subsidence is predicted to be much larger[18], or not anomalous if the crust had not been thinned [20]. If the latter is true, their current deep-water position overlying thin crust is explained by post-deposition faulting, extension and subsidence[20]. In addition, these characteristics may be peculiar to the Newfoundland-Iberia conjugate margins and not typical of Type I margins in general.

Nevertheless, paleobathymetry is an important constraint in the reconstruction of margins and anomalous subsidence requires an explanation. In this regard Model I offers a possible mechanism. From Movie 1 it can be seen that the early evolution is dominated by the rapid subsidence of a symmetric crustal graben keystone block. On the flanks of this block crust is thinned by a factor of 2, which accounts for the large subsidence. Between 12 and 16 *Ma* this keystone is uplifted and disaggregated, and the resulting blocks are tilted, in part by detachment faulting. In particular, the main block becomes subaerial at 16 *Ma* (Movie 1) and the water depth above the up-tilted end of the smaller block is 1500 *m*, similar to that estimated for the chalk. The general uplift coincides with the thinning of mantle lithosphere and its replacement by asthenosphere.

The Model I result has similarities to the inferred evolution of a similar crustal block, the 'H' block, on the Iberia-Newfoundland margin[18]. Although Model I clearly differs in detail from the schematic conceptual model (Fig. 6, Péron-Pinvidic and Manatschal[18]), it does demonstrate how crustal blocks can be elevated by rapid thinning of the lithosphere, uplift of asthenosphere, detachment and rotation. These blocks are not in local isostatic equilibrium and rotation during detachment faulting contributes to the uplift. This anomalous behaviour is not predicted by one-dimensional extension models that are everywhere in local isostatic equilibrium. If similar situations develop in natural systems the bathymetry will not be directly related to local lithospheric thinning. According to our classification, Type I margins are likely to develop this structural style, dominated by large rotated faulted crustal blocks, owing to the cold strong crust.

If our explanation is correct, the key to recognizing this type of shallow bathymetry is that it will occur locally and be associated with the elevated parts of rotated fault blocks. Elsewhere, the subsidence may be in local isostatic equilibrium or even enhanced by downward block rotation.

Type II Margins

Shallow bathymetry and subaerial depositional environments are also observed during syn-rift sedimentation on central South Atlantic margins and the Exmouth Plateau, examples of our Type II margins. Are these conditions produced in the same way as in Model I? We believe not because Type II margins (Models II-A and II-C) undergo more ductile extension, and are less prone to develop large crustal fault blocks that may rotate. Instead, we propose the shallow bathymetry results from the Type II rift style, which places exhumed hot asthenosphere beneath crust that remains relatively thick during much of the syn-rift (Movie 2). The bathymetry may be further reduced by underplating by cratonic mantle lithosphere (Movie 3) as explained in the main text.

Specifically, bathymetry at the Model II-A rift axis evolves such that water depths are < 200 *m* until asthenosphere arrives at the base of the crust (7 *Ma*). Bathymetry then increases slowly reaching 800 *m* (16 *Ma*), 1.2 *km* (26 *Ma*) and 1.6 *km* (36 *Ma*). Where there is sedimentation to sea level on adjacent regions of the margin (Movie 2, <550 *km* and >650 *km*), no more than 7 *km* of sediment (density 2300 kg/m^3) accumulates during the model evolution.

The margin bathymetry of Model II-C also shows a slow increase in depth with rift axis values less than 1 *km* for the first 20 *Ma* and 2.5 *km* at the time of breakup (33 *Ma*). The latter depth coincides with that for oceanic ridges because cratonic underplate has now been removed from beneath the rift axis (Movie 3). The bathymetry in Models II-A and II-C evolves in a similar way because the small depletion density anomaly of the lower cratonic lithosphere (Model II-C), 15 kg/m^3, reduces the bathymetry above thick cratonic underplate by only 391 *m* (local isostatic calculation) by comparison with Model II-A (see main text). However, were the depletion density anomaly 50 kg/m^3, also a permissible estimate, the bathymetry would be reduced by 1304 *m* relative to

Model II-A, which would maintain the rift axis subaerial through at least the first 28 *Ma* of rifting.

We suggest that the Type II rift style combined with variable amounts of cratonic underplate can explain observations of syn-rift subsidence of the central South Atlantic margins and elsewhere, e.g. Exmouth Plateau. Regions with thin crust but no cratonic underplate will subside allowing up to approximately 7 *km* of syn-rift sediment to accumulate (Model II-A type) and this will be shallow water sediment if it fills the available accommodation as it develops. Elsewhere, where there is cratonic underplate the syn-rift subsidence will be reduced in proportion to the increasing depletion density anomaly and thickness of the underplate. We believe this is consistent with the observations which show regions in which the sub-salt syn-rift sediment is either thin to absent (Type II-C) or up to 7km thick (Type II-A) (Garry Karner, pers. comm.).

References:

1   Srivastava, S. P., Sibuet, J.C., Cande, S., Roest, W.R., & Reid, I.R. Magnetic evidence for slow seafloor spreading during the formation of the Newfoundland and Iberian margins. *Earth Planet. Sci. Lett.* **182**, 61-76 (2000).

2   Funck, T. *et al.* Crustal structure of the ocean-continent transition at Flemish Cap; seismic refraction results. *J. Geophys. Res.* **108**, doi:10.1029/2003JB002434 (2003).

3   Murillas, J. *et al.* Structure and evolution of the Galicia interior basin (Atlantic western Iberian continental margin). *Tectonophysics* **184**, 297-319 (1990).

4   Pérez-Gussinyé, M., Ranero, C. R., Reston, T. J. & Sawyer, D. Mechanisms of extension at nonvolcanic margins; evidence from the Galicia interior basin, west of Iberia. *J. Geophys. Res.* **108**, doi: 10.1029/2001JB000901 (2003).

5   Keen, C. E. & de Voogd, B. The continent-ocean boundary at the rifted margin off eastern Canada: new results from deep seismic reflection studies. *Tectonics* **7**, 107-124 (1989).

6   Keen, C. E., Stockmal, G. S., Welsink, H. J., Quinlan, G. & Mudford, B. Deep crustal structure and evolution of the rifted margin northeast of Newfoundland: results from LITHOPROBE. East. *Can. J. Earth Sci.* **24**, 1537-1549 (1987).

7   Dean, S. M., Minshull, T. A., Whitmarsh, R. B. & Louden, K. E. Deep structure of the ocean-continent transition in the southern Iberia abyssal plain from seismic refraction profiles; the IAM-9 transect at 40 degrees 20'N. *J. Geophys. Res.* **105**, 5859-5885 (2000).

8   Torne, M., Fernandez, M., Carbonell, J. & Banda, E. Lithospheric Transition from Continental to Oceanic in the West Iberia Atlantic Margin. in *Rifted Ocean-Continent Boundaries,* eds E. Banda, M. Torne, & M. Talwani, 247-264 (Kluwer Academic Publishers, 1994).

9   Moulin, M. *et al.* Geological constraints on the evolution of the Angolan margin based on reflection and refraction seismic data (ZaiAngo project). *Geophys. J. Int.* **162**, 793-810, doi:10.1111/j.1365-246X.2005.02668.x (2005).

10   Rosendahl, B. R., Mohriak, W. U., Odegard, M. E., Turner, J. P. & Dickson, W. G. West African and Brazilian conjugate margins: Crustal types, architecture, and plate configurations. in *25th GCSSEPM Bob F. Perkins Research Conference: Petroleum Systems of Divergent Margin Basins*, eds Post, P. et al, 261-317 (Houston, 2005).

11   Meyers, J. B., Rosendahl, B. R. & Austin, J. A. Deep-penetrating MCS images of the South Gabon Basin: Implications for rift tectonics and post-breakup salt remobilization. *Basin Res.* **8**, 65-84 (1996).

12   Begg, G. C. *et al.* The lithospheric architecture of Africa: Seismic tomography, mantle petrology, and tectonic evolution. *Geosphere* **5**, 23-50, doi:10.1130/Ges00179.1 (2009).

13   Fullsack, P. An arbitrary lagrangian-eulerian formulation for creeping flows and its application in tectonic models. *Geophys. J. Int.* **120**, 1-23 (1995).

14   Willett, S. D. Rheological dependence of extension in wedge models of convergent orogens. *Tectonophysics* **305**, 419-435 (1999).

15   Huismans, R. S. & Beaumont, C. Symmetric and asymmetric lithospheric extension: Relative effects of frictional-plastic and viscous strain softening. *J. Geophys. Res.* **108**, doi:10.1029/2002jb002026 (2003).

16   Gleason, G. C. & Tullis, J. A flow law for dislocation creep of quartz aggregates determined with the molten salt cell. *Tectonophysics* **247**, 1-23 (1995).

17   Karato, S. I. & Wu, P. Rheology of the upper mantle; a synthesis. *Science* **260**, 771-778 (1993).

18   Péron-Pinvidic, G. & Manatschal, G. The final rifting evolution at deep magma-poor passive margins from Iberia-Newfoundland: a new point of view. *Int. J. Earth Sci.* **98**, 1581-1597, doi: 10.1007/s00531-008-0337-9 (2009).

19   Urquhart, E. Depositional environment of syn-rift sediments on the Iberia margin, *Eos Trans. AGU* **82**, 47, Fall Meeting Suppl., Abstract PP42B-0505 (2001).

20   Ranero, C.R. & Pérez-Gussinyé, M. Sequential faulting explains the asymmetry and extension discrepancy of conjugate margins, *Nature*, **468**, 294-299, doi:10.1038/nature09520 (2010).